



Large-scale trench-normal mantle flow beneath central South America



M.C. Reiss*, G. Rümpler, I. Wölbern

Institute of Geosciences, Goethe University Frankfurt, Altenhöferallee 1, 60438 Frankfurt am Main, Germany

ARTICLE INFO

Article history:

Received 5 July 2017

Received in revised form 30 October 2017

Accepted 1 November 2017

Available online xxxx

Editor: P. Shearer

Keywords:

shear-wave splitting

central Andes

trench-perpendicular mantle flow

crustal anisotropy

ABSTRACT

We investigate the anisotropic properties of the fore-arc region of the central Andean margin between 17–25°S by analyzing shear-wave splitting from teleseismic and local earthquakes from the Nazca slab. With partly over ten years of recording time, the data set is uniquely suited to address the long-standing debate about the mantle flow field at the South American margin and in particular whether the flow field beneath the slab is parallel or perpendicular to the trench. Our measurements suggest two anisotropic layers located within the crust and mantle beneath the stations, respectively. The teleseismic measurements show a moderate change of fast polarizations from North to South along the trench ranging from parallel to subparallel to the absolute plate motion and, are oriented mostly perpendicular to the trench. Shear-wave splitting measurements from local earthquakes show fast polarizations roughly aligned trench-parallel but exhibit short-scale variations which are indicative of a relatively shallow origin. Comparisons between fast polarization directions from local earthquakes and the strike of the local fault systems yield a good agreement. To infer the parameters of the lower anisotropic layer we employ an inversion of the teleseismic waveforms based on two-layer models, where the anisotropy of the upper (crustal) layer is constrained by the results from the local splitting. The waveform inversion yields a mantle layer that is best characterized by a fast axis parallel to the absolute plate motion which is more-or-less perpendicular to the trench. This orientation is likely caused by a combination of the fossil crystallographic preferred orientation of olivine within the slab and entrained mantle flow beneath the slab. The anisotropy within the crust of the overriding continental plate is explained by the shape-preferred orientation of micro-cracks in relation to local fault zones which are oriented parallel to the overall strike of the Andean range. Our results do not provide any evidence for a significant contribution of trench-parallel mantle flow beneath the subducting slab.

© 2017 Elsevier B.V. All rights reserved.

1. Introduction

The subduction of an oceanic plate beneath a stable continent is one of the major geodynamic processes. However, the deformation of the mantle beneath the plates and the resulting flow fields have been subject to a long-standing debate, where two contradicting hypotheses have been put forward: on one hand it is thought that mantle material above and below the subducting plate is entrained by the down-going slab such that the surrounding flow is aligned parallel to the down-dip direction of subduction; alternatively, the slab and the underlying mantle may be decoupled such that the flow beneath the slab aligns parallel to the trench in response to large-scale compressional forces acting along the plate boundary. This can be investigated by the observation of shear-wave splitting, i.e. the splitting of a shear-wave into orthogonally polarized fast and slow components due to seismic

anisotropy. This, in turn, provides direct constraints on the dynamic processes of earth's interior as seismic anisotropy is thought to be caused by the response of crustal and mantle materials to strain. In the mantle, anisotropy is usually due to the crystallographic preferred orientation (CPO) of olivine (Savage, 1999; Long and Silver, 2009b), the main constituent of the upper mantle. Using an experimental set-up with simple shear, which is most likely the dominant mode of deformation in the upper mantle, Zhang and Karato (1995) showed that the a-axis of olivine aligns in the direction of flow for large strains assuming relatively dry conditions. In the crust, alternating sedimentary layers or oriented cracks cause shape-preferred orientation (SPO) of anisotropy (Crampin, 1994; Park and Levin, 2002). The orientation and strength of an anisotropic fabric can be inferred from the polarization of the fast-wave component (ϕ) and the delay time (δt) between fast and slow components, respectively.

In this context, subduction zones yield a complex signal of shear-wave splitting as the mantle flow beneath the slab, the slab itself, the mantle wedge and the overriding plate may all

* Corresponding author.

E-mail address: reiss@geophysik.uni-frankfurt.de (M.C. Reiss).

contribute different anisotropic signatures (Long and Silver, 2008, 2009a; Long et al., 2016). During plate formation at the mid-ocean ridges, the mantle flow produces CPO parallel to the spreading direction which is then ‘frozen-in’ as the plate cools (Hess, 1964; Becker et al., 2014). Additionally, the rigid movement between the plate and upper mantle can cause significant CPO parallel to plate motion (Savage, 1999). During the subduction process, the mantle flow field and thus the anisotropic pattern may be affected by the retrograde motion of the subducting slab, trench migration and geometry of the slab itself (Russo and Silver, 1994; Long and Silver, 2008; MacDougall et al., 2012).

In the fore-arc region, additional mineralogical and geodynamical constraints must also be considered. Faccenda et al. (2008) suggests that a combination of CPO and SPO develops in the slab from hydrated faults and serpentinized minerals. Furthermore, the relationship between flow and alignment of the olivine *a*-axes may not be as simple as previously suggested. While the A-type olivine may form in low stress and dry conditions, Jung and Karato (2001) demonstrated that temperature, pressure, and water content have a significant impact on the development of the slip system. For subduction systems, B-type olivine, which has a fast axis perpendicular to the flow direction, may be prevalent in the fore-arc region in a water-rich mantle (e.g. Ohuchi et al., 2012). Both mechanisms lead to trench-parallel fast polarizations, while the flow remains aligned with the down-dip direction. Above the slab, a possible two-dimensional corner flow within the mantle wedge is conceivable, which is induced by the downward motion of the slab (Long and Silver, 2009a) and causes olivine crystals to align parallel to the plate motion.

The South American margin was one of the first regions where trench-parallel flow due to retrograde motion of the slab combined with a flow barrier at depth was proposed (Russo and Silver, 1994). Shear-wave splitting results yielded fast polarization directions which were mostly interpreted to be trench-parallel with the exception of three confined areas, of which one was explained by a stagnation point of the mantle flow field. In a later study, a 150-km wide stagnation zone, centered at $\sim 18^\circ\text{S}$, was proposed (Polet et al., 2000). Since then, many more studies along the Nazca subduction were carried out (Bock et al., 1998; Anderson et al., 2004; MacDougall et al., 2012; Hicks et al., 2012; Eakin and Long, 2013; Wölbern et al., 2014; Eakin et al., 2015, 2016; Long et al., 2016). While the concept of trench-parallel mantle flow beneath subducting slabs became accepted and many studies reported trench-parallel polarizations, the growing number of observations often yielded more complex splitting patterns which could not be reconciled with simple mantle flow models or one layer of anisotropy.

Wölbern et al. (2014) reported mostly trench-perpendicular fast polarizations of SKS phases along a seismic profile in the Central Andes at $\sim 21^\circ\text{S}$ which were interpreted due to fossil anisotropy in the slab. Others have argued for an overprinting of the fossilized slab fabric by extension further by analyzing deep local S phases (Eakin et al., 2016). Most recently, trench-parallel mantle flow beneath subducting slabs has been questioned by a study of world-wide source-side splitting measurements, which utilize the ray paths of slab events traversing the slab mantle and are uncontaminated from anisotropic structures above the slab. The study finds that the measurements are best characterized by tilted transverse isotropy with a slow symmetry axis orthogonal to the slab dip and that trench-parallel fast polarization directions are associated with relatively shallow events (Walpole et al., 2017).

In our study, we analyze data from 21 stations of the IPOC network (GFZ, 2006) which are located between 17° – 25°S and directly situated in the fore-arc (Fig. 1). This data set is uniquely suited for the analysis of shear-wave splitting in this region as it covers a range of 780 km along the central South American margin, extending about 160 km east–west and most of the seismic

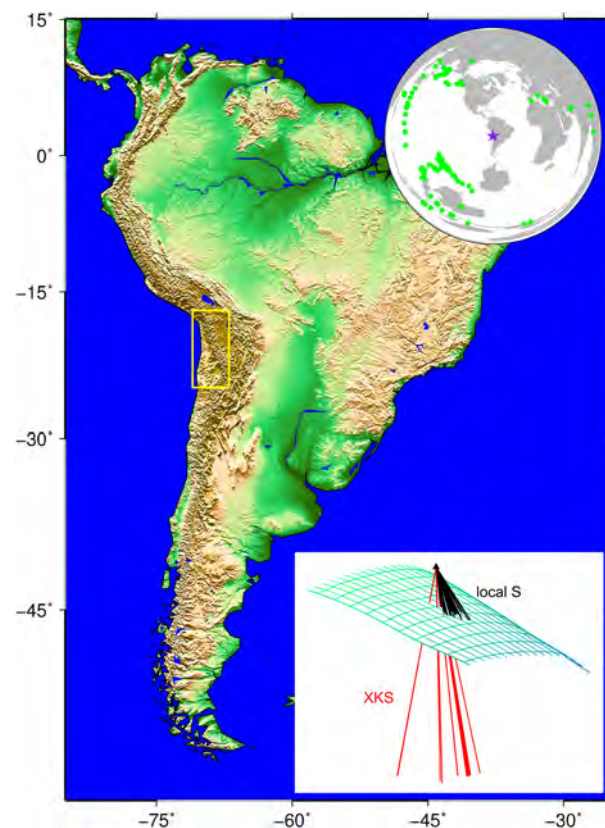


Fig. 1. Map of South America with the study area highlighted in yellow. The upper inset shows the distribution of the teleseismic events used in the study. The lower inset shows a sketch of the ray paths through the subduction system. Teleseismic ‘XKS’ phases traverse the entire subduction zone nearly vertically, while local S phases originate in the slab and have shallower incidence angles. (For interpretation of the references to color in this figure legend, the reader is referred to the web version of this article.)

stations have been in operation for more than 10 yrs. We use teleseismic and local S phases to investigate the anisotropic properties and sample different parts of the subduction zone (Fig. 1, lower inset). We constrain two anisotropic layers which yield important findings for the mantle flow pattern. Furthermore, we test the influences of anisotropy within the crust upon the teleseismic measurements by using a two-layer inversion of all waveform data at one given station.

2. Methods

The Integrated Plate boundary Observatory Chile (IPOC, GFZ, 2006) consists of 21 stations in northern Chile between 17° – 25°S . This is a permanent station deployment with ongoing data acquisition. About half of the stations started recording in 2006 and now have 10 yrs of data available while the remainders were successively installed in the years after.

We use the SplitRacer software package (Reiss and Rümpler, 2017) to measure teleseismic shear-wave splitting by minimizing the transverse energy (see Silver and Chan, 1991). We analyze data from teleseismic earthquakes between 85° – 180° distance to include all core phases such as SKS, SKKS and PKS (called XKS in the following). A minimum event magnitude of 6 of the USGS earthquake archive was used to find suitable events. We conduct the entire processing flow for two filter ranges: As most teleseismic core phases have a period of ~ 8 – 12 s, we first use a traditional bandpass filter of 4–50 s for the analysis. As evidence for depth-dependent anisotropy can be also observed by using different frequency bands (Rümpler et al., 2003), we repeat our analysis using a bandpass filter of 1–4 s, which is comparable to the fre-

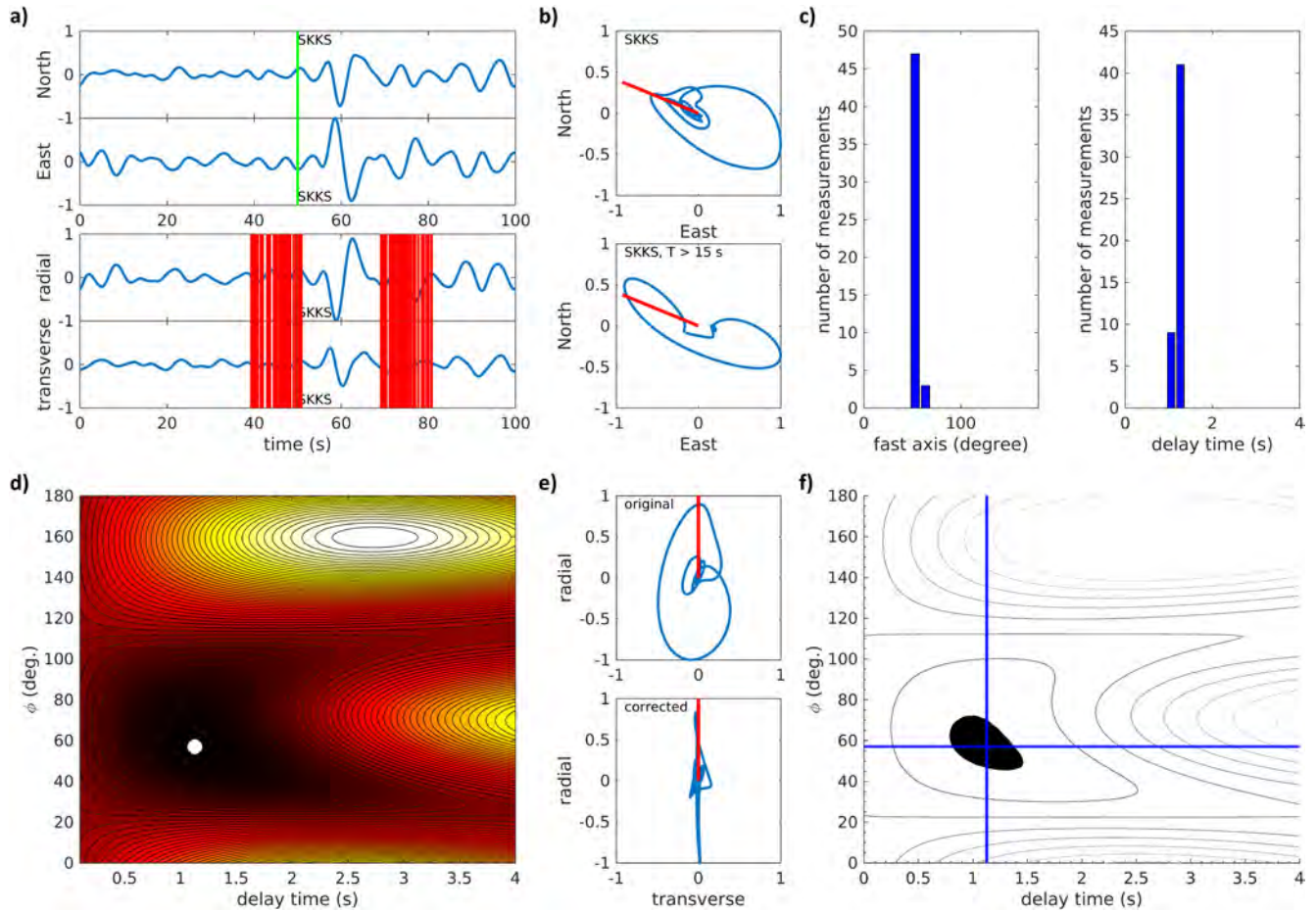


Fig. 2. Example of teleseismic single phase shear-wave splitting measurement at station PB04 (8th of November 2011). a) North/East and radial/transverse components. The theoretical phase arrival is denoted by the green bar, the 50 different time windows used for the analysis are shown in red. b) Particle motions for only the originally chosen phase (here: SKKS) time window, and the original time window using a low pass of 15 s. The red line is the theoretical backazimuth. c) Histogram of all measurements. d) Transverse-energy grid with averaged splitting parameters denoted by the white dot. e) Original and corrected particle motion shown. f) 95% confidence level atop the energy grid. The blue cross indicates the splitting parameters. (For interpretation of the references to color in this figure legend, the reader is referred to the web version of this article.)

quency content of local S phases from the slab. A signal-to-noise ratio (SNR) of 2 was chosen to automatically select suitable phases of an event with a clear phase onset. Phases were additionally inspected visually during pre-processing and time windows for the analysis manually altered if necessary. We repeated the measurement for 50 randomly-chosen slightly different time windows to probe the robustness of the measurements.

For teleseismic core phases, the initial polarization is readily known from the backazimuth of the event. The difference between the theoretically calculated backazimuth and the long axis of the long-period filtered particle motion can be used to correct possible sensor misalignments (Reiss and Rumpker, 2017). During pre-processing, we calculate misalignment values for all phases per station. If the misalignment values are independent of time, we calculate a mean sensor correction value and apply it before the calculation of splitting parameters. On average, the station misalignment was $\sim 4^\circ$ with a maximum misalignment value of $\sim 9^\circ$. For the splitting measurement, north and east components of each phase are rotated into radial and transverse components. Then, a grid search for the splitting parameters ϕ (fast polarization) and δt (delay time) is performed which returns one pair of splitting parameters which, used as an inverse splitting operator, best reduces the energy on the transverse component. For each splitting measurement, we consider the amount of energy reduction on the transverse component and check the correction of the particle motion visually. If the splitting parameters characterize the

anisotropic properties beneath the station, the particle motion becomes linear when applying the inverse splitting operator (Reiss and Rumpker, 2017; see Fig. 2 for an example).

If anisotropy is not present or whenever the polarization of the incoming wave aligns with the fast (or slow) axis of the anisotropic medium the measurement is termed ‘null’. When more than one horizontal anisotropic layer is present, both splitting parameters display a distinct 90° -periodicity with the initial polarization of the incoming wave (Silver and Savage, 1994; Rumpker and Silver, 1998). If the fast orientations of two anisotropic layers are perpendicular to each other, they can cancel each other out, if their individual signatures are of similar strength.

In addition to the single phase splitting measurements, we use the single-layer and two-layer joint splitting inversion (Reiss and Rumpker, 2017). Our work flow is as follows: all (full) waveforms per station which previously produced splitting measurements (splits and nulls) are used in the one-layer inversion if single phase measurements are not significantly dependent on the backazimuth, and in the two-layer inversion if their dependency upon backazimuth is evident. In the inversion for one layer, we calculate the energy grid in the same manner as for a single phase splitting measurement, but stack it for each phase. This is similar to the approach of Wolfe and Silver (1998). The minimum value of this stacked energy grid for all participating waveforms alike yields the one pair of splitting parameters ϕ and δt which, used on the original waveforms, best reduces the transverse en-

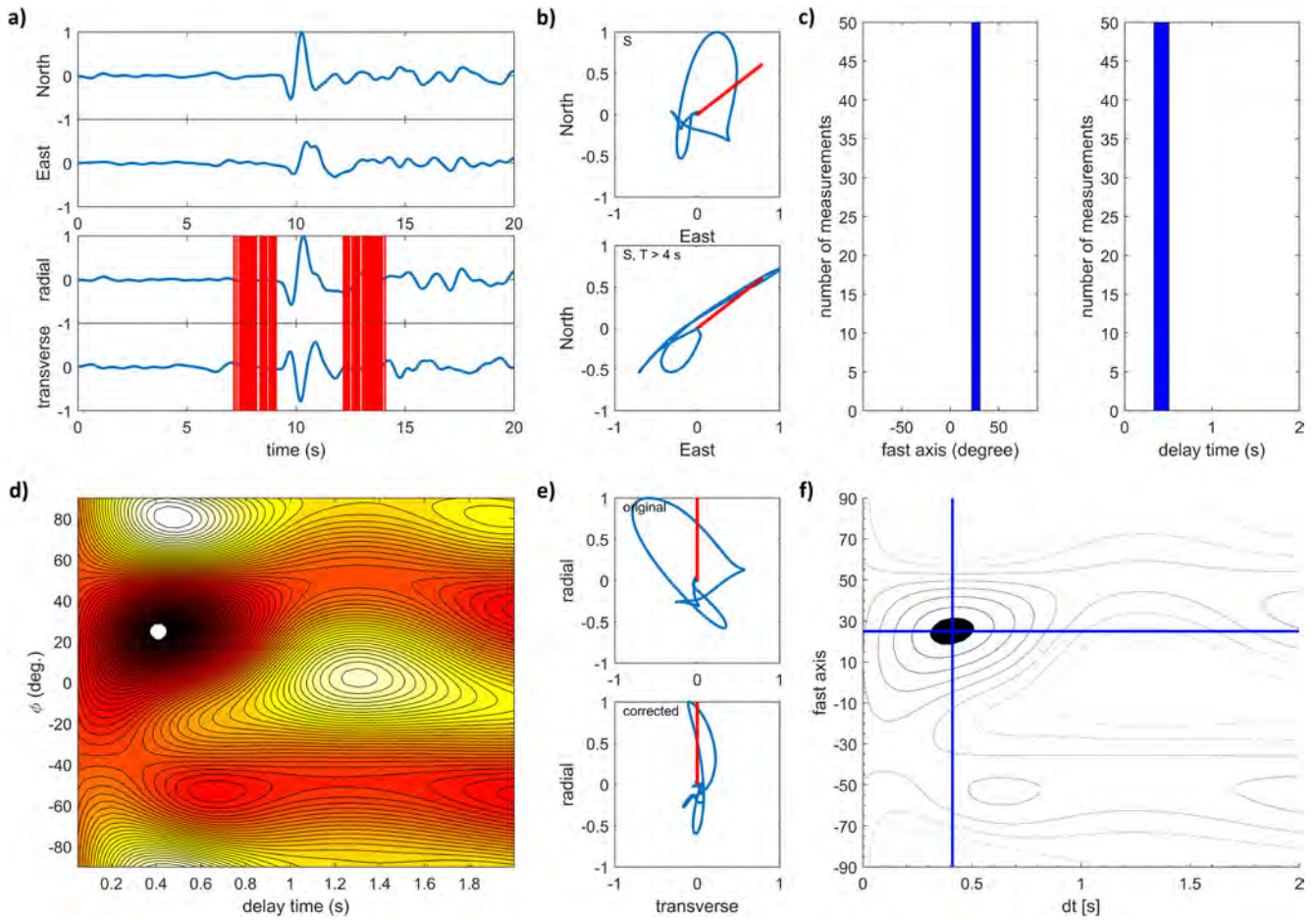


Fig. 3. Example of local S single phase shear-wave splitting measurement at station PB09 (20th of May 2012). a) North/East and radial/transverse (with respect to the initial polarization) components. The 50 different time windows used for the analysis are shown in red. b) Particle motions for the originally chosen time window with a filter of 1–4 s, and the same time window filtered by a low pass of 4 s. The red line is the initial polarization as estimated from the long axis of the long-period filtered particle motion. c) Histogram of all measurements. d) Transverse-energy grid with averaged splitting parameters denoted by the white dot. e) Original and corrected particle motion shown. f) 95% confidence level atop the energy grid. The blue cross indicates the splitting parameters. (For interpretation of the references to color in this figure legend, the reader is referred to the web version of this article.)

ergy on all phases simultaneously. This is asserted by calculating the amount of transverse-energy reduction and visually checking whether the particle motions become linearized when applying the splitting pair. To probe the statistical robustness of the measurement, we also use 50 slightly different time windows and repeat the analysis for each. We check the consistency of these results by evaluating a histogram. This inversion procedure reduces the influence of noise and increases the robustness of the measurements (Reiss and Rumpker, 2017). In the two-layer inversion, an additional grid search is applied to constrain the properties of a possible second anisotropic layer. Thus, each individual point in the transverse-energy grid is then dependent upon four parameters. In view of computational constraints, we repeat these measurements for 5 slightly shifted time windows only but otherwise the procedure is the same as for the one-layer inversion (Reiss and Rumpker, 2017). Similarly, Özalaybey and Savage (1994) used a two-layer grid search on single waveforms and then stacked the transverse energy misfit spaces.

We alter the used software to analyze local S phases from the slab. For this, we only use events with incidence angles less than 30° to avoid contamination from surface-refracted and reflected phases. We use slab events with magnitudes greater than 3 and reduce the pre-processing procedure to a visual inspection only. We adapt the filter settings manually to enhance the SNR for each phase. We also integrate the time series which is the same as applying a restitution to calculate the initial displacement. Used

bandpass ranges are between periods of 0.1–6 s. As the initial polarization of the phase is not known from the backazimuth, we use the long axis of the long-period filtered particle motion to estimate the initial polarization (see Rumpker and Silver, 1998). Depending on the frequency content of the waveform, the cut-off for the long-period filter varies between 1–6 s. The procedure for calculating the single phase splitting measurements is the same as for the teleseismic phases (see Fig. 3, Table A4).

3. Results

3.1. Teleseismic shear-wave splitting analysis

First, we determine the splitting parameters for every XKS phase at every station by applying the transverse energy-minimization method separately to each phase (single-phase splitting results). For the bandpass filter of 4–50 s, a total of 118 events fulfilled the chosen criteria which yielded 459 measurements (Fig. 4, Table A1). On average, this yields a fast polarization of $83 \pm 24^\circ$ and a delay time of 1 ± 0.4 s (Table A1). The bandpass filter of 1–4 s yielded 441 measurements from 117 events (Fig. A2, Table A2). Average fast polarizations are $84 \pm 20^\circ$ and $\sim 0.8 \pm 0.3$ s delay time, respectively (delay time averages are calculated without null-measurements). While there is some evidence for frequency dependence of splitting measurements (Fig. A3), there are no fundamental changes of observed splitting. Hence, we continue to refer only to those measurements filtered by 4–50 s.

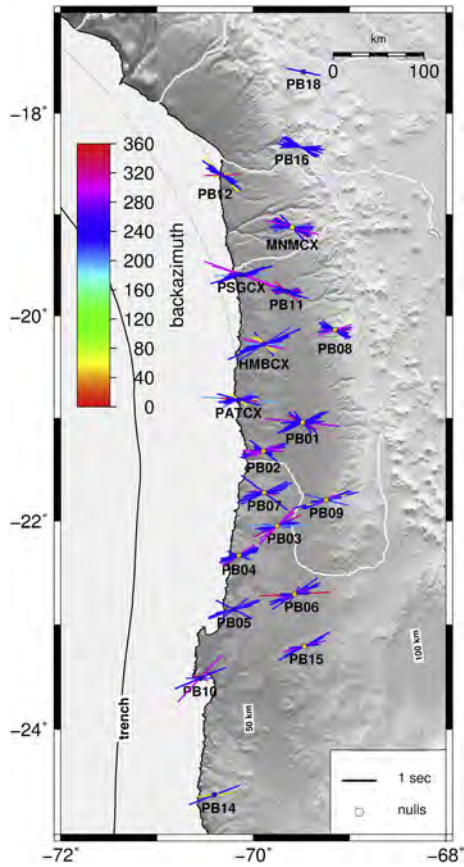


Fig. 4. Map of teleseismic single phase splitting results, band-pass filtered between 4–50 s. Results are centered on the station coordinates and are color coded by backazimuth. The gray contour lines mark the depth of the subducting Nazca slab (Cahill and Isacks, 1992). (For interpretation of the references to color in this figure, the reader is referred to the web version of this article.)

Next, we examine whether these results depend on backazimuth. Given the standard deviations from averaged splitting parameters as well as the visualization of results in Fig. 4, the single phase splitting results reveal some scattering of fast polarizations and delay times. Variations of splitting parameters with backazimuth can be indicative of layered anisotropy, which then display a 90°-periodicity (Silver and Savage, 1994; Rumpker and Silver, 1998). To analyze this, the fast polarization and delay time have been plotted over the backazimuth for all stations (see Fig. A3). Additionally, results have been color coded by their backazimuth in Fig. 4. The analysis of backazimuthal dependence is somewhat limited as the data set is dominated by events from the Tonga–Fiji subduction zone. While some stations have rather limited backazimuthal coverage (e.g. PB16, PB05), others have reasonable coverage of different backazimuths (e.g. HMBCX, PATCX, PB01). Stations with reasonable coverage display some variations with backazimuth, although there is also smearing of results for the same backazimuth for many stations, i.e. slightly different fast polarization values for the same backazimuth.

As single-phase splitting measurements are prone to noise, we also apply a joint inversion which utilizes all XKS phases at a station. On average, 23 phases were used per station in the inversion (see Table A3 for more details). Given the backazimuthal limitations and difficulties to identify variations with backazimuth, we employ both the one and two-layer joint-inversions. First, we use the hypothetical one-layer joint splitting inversion. Given the overall reduction of energy on the transverse components and the correction of the particle motion, this approach seems suitable for all stations (see Fig. 5 for results). The resulting fast polarizations for the one-layer inversion are oriented approximately East–West

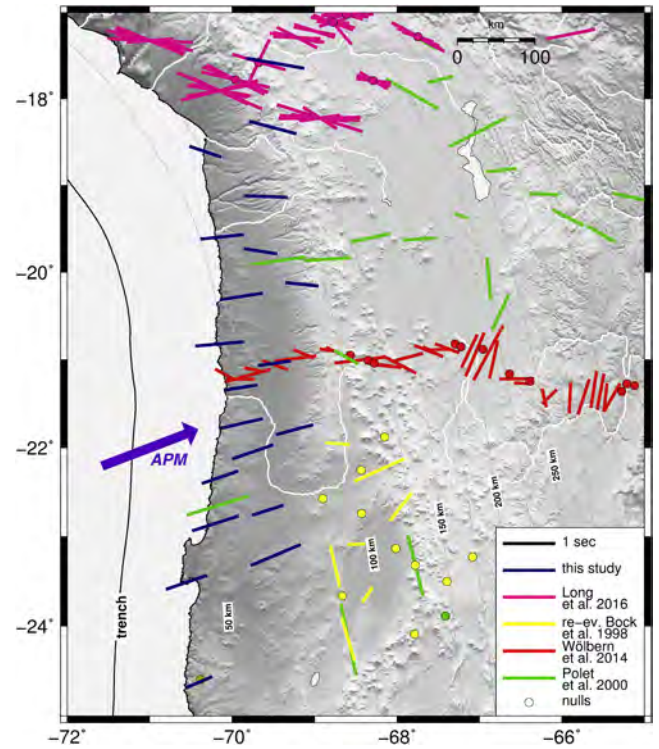


Fig. 5. Map of joint splitting results for the teleseismic phases. Results are centered on the station coordinates. To compare our findings to previous studies, we also show the measurements of Long et al. (2016), Bock et al., 1998 (re-evaluated results by Wölbern et al., 2014), Wölbern et al. (2014) and Polet et al. (2000). The purple arrow denotes the absolute plate motion while gray contour lines mark the depth of the subducting Nazca slab (Cahill and Isacks, 1992). (For interpretation of the references to color in this figure legend, the reader is referred to the web version of this article.)

and exhibit an average angle of $83^\circ \pm 13^\circ$, the average delay time is 0.8 ± 0.2 s (Fig. 5). There is a clearly visible change in the orientation of the fast polarizations directions from North to South. In the South, fast polarizations are distinctly uniform ENE at approximately 75° which is parallel to the absolute plate motion (APM). In the North, fast axes are slightly less uniform but show a clear trend towards ESE at approximately 100° . The change in fast polarization directions seems to coincide with the curvature of the trench which is oriented $\sim 0^\circ$ in the south and begins to curve towards NW at 21° S. The gradual change of fast polarizations is centered here. For the northernmost stations, the strike of the trench is $\sim 30^\circ$ NW.

As the single-phase splitting analysis is inconclusive to vertically-varying anisotropy, we test this by also inverting the data at each station for two anisotropic layers simultaneously. However, this station does not yield reasonably stable inversion results for most stations, as the splitting parameters vary for slightly different time windows (see Fig. A4). Only stations PATCX, PB16 and PB18 yield results which provide a higher transverse-energy reduction compared to the one-layer inversion. However, station PB18 has only two measurements and station PB16 has no backazimuthal coverage. Station PATCX has a reasonable backazimuthal coverage for which the two-layer inversion yields a lower layer of 75° and 1 s and an upper layer with 120° and 0.2 s for the fast polarization and delay time, respectively. As the joint inversion for two anisotropic layers is largely unsuccessful, we have to assume the results provided by the one-layer inversion are representative of the bulk anisotropy sampled by the teleseismic phases. A possible interference from another anisotropic layer is suspected, but cannot be substantiated on the basis of the teleseismic measurements alone.

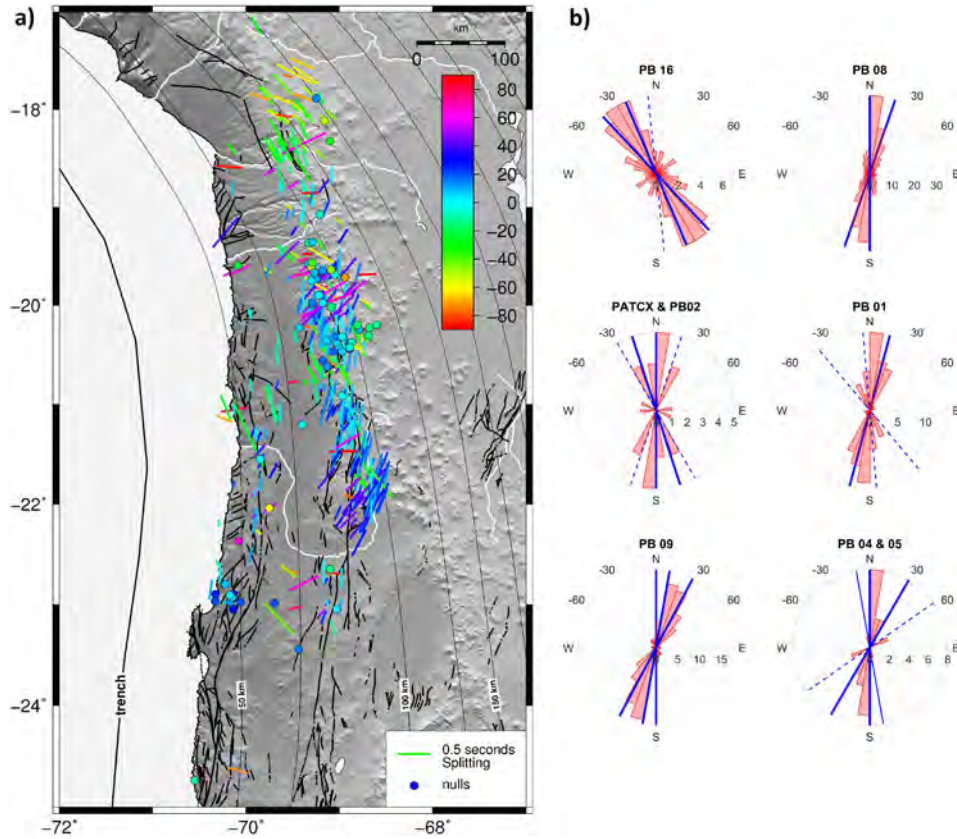


Fig. 6. a) Map of local S splitting measurements. Results have been plotted atop the earthquake source locations for better visibility. Gray lines indicate the depth to the subducting Nazca slab. Solid black lines denote faults zones and the trench (Reutter and Munier, 1994; Garcia et al., 2004; Vellozo et al., 2012; Charrier et al., 2013). Splitting parameters are colored according to their fast polarization direction for better readability and scaled by their delay time. b) Rose diagrams of the distribution of fast polarization directions for selected stations. Red wedges denote the frequency of fast polarizations in 10° bins, while blue lines are the strikes of faults in the vicinity of the respective station. Solid lines indicate major faults, dashed lines minor faults. (For interpretation of the references to color in this figure legend, the reader is referred to the web version of this article.)

3.2. Local S shear-wave splitting

The analysis of S phases from local earthquakes yields 441 measurements with strong and partly short-scale variations from North to South across the study area (Fig. 6a). The average delay time is 0.3 ± 0.15 s. In the North, between 17°–19°S, fast polarizations are mostly NWN at $\sim -30^\circ$. Fast polarization directions are (sub) parallel to each other along at least 1° latitude. To characterize the results further, rose plots for individual stations are plotted next to it. These show the frequency of the fast polarizations binned in 10° wedges (see Fig. 6b, station PB16). Stations were chosen to give a good spatial distribution across the study area and include those stations with many local S measurements. In the center, fast polarizations scatter with many partially coherent orientations around -30° , 0° and $\sim 30^\circ$, which may be indicative for localized variation in seismic anisotropy (see Fig. 6b, stations PB08, PATCX and PB02, PB01). The variable fast polarization directions are accompanied by many null-measurements and slightly smaller delay times compared to the northern and southern regions. As the immediate surroundings are seismically anisotropic, the null-measurements do not seem to be indicative of isotropic regions. A more likely explanation for this is that the corresponding initial polarizations and the anisotropic fast axis directions are relatively similar or highly localized differences between anisotropic fabrics may cancel each other out. In the south, between 21°–24°S, fast polarizations are mostly between 10° – 30° and display strong parallel alignment (see Fig. 6b, stations PB09, PB04 and PB05).

On first glance, the fast axis directions from the local events seem to align parallel to the trench. In particular, the northern

and coastal areas display a profound resemblance, whereas measurements of fast-axis directions between 21°–23°S exhibit large deviations of up to 40° from the orientation of the trench. However, the measured fast axes directions fit well to the strikes of local fault zones for the entire study area (Fig. 6), which suggests a relationship. To show this resemblance, we estimated the strikes of the fault zones and added them to the roseplots in Fig. 6b. Given the quantity of fault zones, we plot only those which lie between the station and earthquake source. Solid lines are indicative of major faults as estimated by the length and the number of similar faults in the vicinity. Dashed lines represent isolated or less prominent faults.

Overall, there is little evidence for depth-dependence among the local S delay times except for station PB01, where delay times increase linearly with depth when ray paths are longer than ~ 110 km (see Fig. A5). For all other stations, delay times seem to be independent of the earthquake source depth and ray path lengths (see Fig. A5). The depth distributions of events of the stations next to PB01 are very similar but do not display the same dependency. Results are also independent of initial polarization but vary with backazimuth at some stations which points towards a stronger local heterogeneity of the anisotropic fabric.

4. Modeling

4.1. Modeling of apparent splitting parameters

The local S splitting results indicate an anisotropic fabric different to the one measured by the teleseismic phases. The teleseismic

Table 1

Joint inversion results for a fixed upper layer.

Station	Fixed upper layer		Inversion result for lower layer	
	ϕ (°)	δt (s)	ϕ (°)	δt (s)
HMBCX	0	0.3	85	1.1
	−20	0.3	80	1.1
PATCX	−30	0.4	75	1.4
	−18	0.4	75	1.4
PB01	0	0.4	85	1.4
	19	0.4	95	1.2
	15	0.5	95	1
	−5	0.5	85	1.1
PB02	−30	0.4	70	1.1
	−18	0.4	80	1
PB04	0	0.4	85	1
	19	0.4	95	0.9
	−10	0.3	75	1
	0	0.3	75	1
PB05	30	0.3	85	0.7
	−10	0.3	85	1.1
	0	0.3	75	1.2
PB08	30	0.3	85	0.9
	0	0.4	95	1
PB09	19	0.4	105	1
	0	0.5	80	1.2
PB16	10	0.5	85	1.1
	28	0.5	90	0.9
	−43	0.5	85	1.1
	−23	0.5	90	1.4
	−6	0.5	95	1.5

single phase splitting measurements demonstrated some degree of backazimuthal dependence whose significance remained inconclusive with respect to the two-layer inversion. We now try to exploit this backazimuthal dependence by testing the resemblance between our measured data and the expected 90°-periodicity of apparent splitting parameters with backazimuth for two anisotropic layers (Silver and Savage, 1994; Rumpker and Silver, 1998). We assess this by using SplitRacer's forward modeling of apparent splitting parameters resulting from two anisotropic layers at depth (Reiss and Rumpker, 2017). For each station, we calculate 46656 models, for which the layer parameters are varied by 10° and 0.2 s for the fast polarization and delay time, respectively. We use a least-squares approach to find the ten two-layer models that best reproduce our observed splitting parameters. Considering the ten best-fitting models per station, we observe wide scattering of possible two-layer models for most stations which indicates the non-uniqueness of the fits to the data (Fig. A6). Thus, a unique model cannot be inferred from this approach.

4.2. Joint inversion with fixed upper layer

Given the inconclusiveness of the two-layer inversion, we test the possibility to isolate a lower anisotropic layer from a joint inversion of all teleseismic waveforms at a given station by keeping the anisotropic parameters for the upper layer fixed. This approach is similar to the joint inversion for two layers described in the Methods section. However, it reduces the inversion problem to only two parameters. Given the high degree of similarity between the strike of local faults and the observed fast polarizations of local S phases, we assume that the anisotropy in the upper layer can indeed be characterized by the orientations of the fault zones. As a proxy, we use the estimated strike of faults for selected stations which have many local S measurements (shown in Fig. 6b) and perform the inversion for these stations and an additional station with good backazimuthal coverage (HMBCX). For each station, we fix the fast axis in the upper layer to the strike direction and take the corresponding delay time from a dominant delay time measured from the local S splits in the vicinity of the station (be-

tween 0.3–0.5 s). For all stations, more than one fault is present whose strikes range between −43° and 28° with median of 0° (see Table 1). Thus, we repeat the inversion for each strike, while the delay time is always fixed to the same value. For the lower layer, the resolution of the search grid is 5° for the fast axis, which ranges from 0–180°. The delay time is varied between 0–2 s with increments of 0.1 s. Each inversion is repeated for 5 slightly altered analysis time windows to ensure that the results are stable.

Table 1 summarizes the results of the two-layer joint inversion and explicitly states all fixed upper-layer parameters for each station. The inversion results for the lower layer vary between 75–105° and 0.7–1.5 s for the fast polarization and the delay time, respectively. On average, the inversion yields a fast polarization of 85 ± 8° and a delay time 1.1 ± 0.2 s. For all stations, the fast axis of the lower layer is roughly ~80° when the upper layer is set to NW or N fast polarizations. If the fast axis of the upper layer is set to NE directions, the lower layer fast axes are ~90° and delay times slightly decrease.

4.3. Comparison between different lower layer models

The joint inversion with a fixed upper layer provides a lower layer with rather uniform properties for all stations. However, we additionally test whether modeled apparent splitting parameters resulting from 2-layer models with different lower layers, i.e. APM parallel (~70°) and parallel to the trench (between −30° and 0° depending on the station location) can fit the observed teleseismic splitting data better than those obtained from the inversion which yielded ~85°. We analyze the same stations for which we calculated the joint inversion with a fixed upper layer. For each station, the upper layer is set to the same parameters as in the inversion process to mimic anisotropy from fault zones, i.e. if we estimated two fault strikes, we calculate 6 models. We use a mean value of 1.1 s for the delay time of the lower layer (see Table A5) and calculate apparent splitting parameters for a backazimuthal range of 360°. To assess the fit between the apparent splitting parameters and the observed data, we calculate the percentage of single phase splitting measurements for which the model lies within the measurements' error bars. As we cannot predefine which fault zones are most dominant on the teleseismic measurements, we sum the fits for one station over all upper layer models for one given lower layer. Thus, the amount of data fit by the calculated percentage value determines how the entirety of combinations between a fixed lower layer and several upper layers fit the observed data (see Table A5 for all parameters and results).

To illustrate these results, Fig. 7 shows an example for station PATCX, for which we estimated four different strike directions (see Fig. 6b) and thus four upper layers (as denoted by four sets of apparent splitting parameters signified by the different colors of solid lines). As visible, the single splitting measurements are fitted best by those models where the lower layer is set to the inversion results (~85°) with 65% and 74% for the fast polarization and delay time, respectively. The models with an APM parallel lower layer fit some of the data (26% of fast polarizations and 47% of the delay times) while the models with the trench-parallel lower layer (here 0°) fit none of the observed fast polarizations and 36% of the delay times (see Table A5). Station PATCX is exemplary for all others stations, as the percentage of fit observed measurements is always the highest for those apparent splitting parameters resulting from a model where the lower layer fixed to the inversion values, while the APM parallel lower layer fits some of the fast polarizations and delay times. The models with the trench-parallel anisotropy in the lower layer fit nearly none of fast polarizations, while for some stations, the delay times are rather well matched (see Table A5).

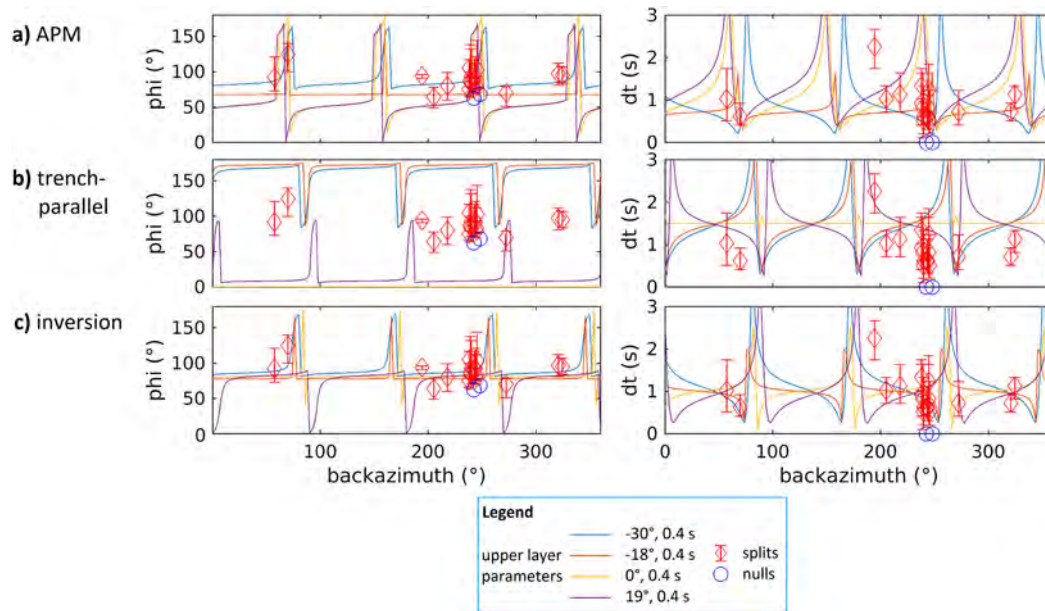


Fig. 7. Comparison between modeled apparent splitting parameters resulting from different two-layer models and observed teleseismic single phase splitting results for station PATCX. Red diamonds with error bars denote measured splitting parameters and blue circles denote measured nulls. Each model consists of two anisotropic layers. The upper layer mimics the fault zones in the vicinity of the stations; parameters are given by the color legend. The lower layer parameters vary; in a) it is set to 70° and 1.1 s for all four models, in b) it is set to 0° for all four models and in c) the inversion results are used so that the lower layer is set to 75° and 1.4 s for the first two models, to 85° and 1.4 s for the third and 95° and 1.2 s for the fourth model. (For interpretation of the references to color in this figure legend, the reader is referred to the web version of this article.)

5. Discussion

5.1. Depth distribution and sources of anisotropy

Our teleseismic and local S measurements suggest different anisotropic fabrics. The ray paths of the XKS and local S phases probe different parts of the subduction system which allows to constrain the depth and spatial distribution of the anisotropic regions to some extent. The teleseismic phases sample the entire subduction system at a steep angle (with average incidence angles of 8.6°), while we allow up to 30° incidence angle from local S phases. As teleseismic shear-wave splitting measurements yield path-integrated results (Long and Silver, 2009b), the splitting parameters may exhibit variations with frequency and backazimuth due to lateral and vertical variations of anisotropy as evidenced by our single-phase splitting results. From the teleseismic data, we were not able to directly infer two anisotropic layers using the observed measurements or waveforms, which may partly be due to the limited backazimuthal distribution of the events and/or due to the heterogeneity in the upper layer. Using the results of local S phases to constrain an upper anisotropic layer, we are then able to infer the parameters of the second layer. Thus, we first consider the measurements of local S phases which characterize an upper anisotropic layer. Using the slab contours derived from local seismicity (Cahill and Isacks, 1992), we estimate our stations to be situated about 50–100 km above the slab surface with increasing depth from West to East. Assuming that most local S phases originate in the upper part of the subducting slab, their ray paths mostly sample the overriding plate which has been estimated to exhibit a 60–70 km thick crust (Wölbern et al., 2009; Sodoudi et al., 2011). North of 20°S, the trench displays a distinct curvature which coincides with a steeper subduction angle of the Nazca plate. Here, local S phases may also sample a significant portion of the mantle wedge. However, the results from local S phases indicate that shear-wave splitting results are independent of the source depth and their location from the trench and also show small-scale variations. This is indicative of a relatively shal-

low anisotropic region, located most likely within the crust. Crustal anisotropy has been noted before (e.g. Savage, 1999) but is often considered to be a local phenomenon and less significant for teleseismic shear-wave splitting observations (Silver and Chan, 1991; Fouch and Rondenay, 2006).

The measured fast polarizations fit well to the strikes of local fault zones for the entire study area (Fig. 6), which suggests a relationship. Seismic anisotropy in the upper crust is likely caused by the shape-preferred orientation of fault-zone related cracks (Crampin, 1994). Assuming that brittle deformation is confined to the upper 20 km of the crust, 5.1% of anisotropy is necessary to explain the average value of the observed delay times. Support for this interpretation also comes from receiver function images at 21°S which trace main fault zones to depth (Wölbern et al., 2009). A recent magnetotelluric study also shows structural anisotropy in the crust with a preferential direction of the electrical conductivity parallel to the strike of the fore-arc thrust fault system (Brasse and Eydum, 2008). Additionally, the lower crust may develop a significant CPO (Ko and Jung, 2015), which could be explained considering the crustal shortening experienced by the overriding plate due to pure and simple shear mechanisms in the context of the subduction process (Allmendinger and Gubbels, 1996). However, we cannot differentiate between these mechanisms on the basis of our measurements alone.

The local S measurements also partly traverse the mantle wedge. Assuming that the preferred alignment of crystals is preferentially due to dislocation creep (Karato and Wu, 1993), anisotropy in the mantle is limited to the upper 400 km. Shear-wave splitting is usually interpreted to result from mantle anisotropy due to preferentially aligned olivine crystals. In subduction systems, the mantle wedge often plays an important role as anisotropy can occur due to a number of mechanisms. A classical 2D corner flow is expected to align the olivine a-axis in the direction of flow under normal conditions, while the serpentinization of the mantle wedge or a change in the olivine slip system can produce trench-parallel fast polarization directions for this part of the subduction system (Long and Silver, 2008; Sodoudi et al., 2011;

Bostock et al., 2002; Ohuchi et al., 2012). If these processes were at play, delay times should be significantly larger in the North, where the ray paths sample a much larger portion of the mantle wedge compared to the central and southern stations.

At station PB16, we observe a few local S measurements with slightly larger delay times than the estimated average. Considering the strike of the local faults close to station PB16 in the North and the strike of the trench, which are parallel to subparallel and splitting delay times should add up, this may signify a contribution of 0.1–0.2 s from the mantle wedge. However we observe similar delay times for stations close to the coast, where the mantle wedge is virtually absent, and closer inland. Thus, this effect may be limited to the northern part of our study area. Large delay times may also be caused by sufficiently deep local faults and/or a significant CPO at depth. A 2D corner flow would align the a-axis of the minerals close to the trench more-or-less vertically and mostly trench-perpendicular in the remainder of the fore-arc. This should cause large variations in delay times and possibly fast polarization directions. As the observed delay times are very similar throughout the region, with some exceptions noted before, a different cause seems more likely.

The entire slab and underlying mantle are only traversed by the teleseismic phases. The slab material is thought to have a fossil anisotropic fabric resulting from the time of plate formation (Hess, 1964; Becker et al., 2014). This is approximately the same as the current APM direction of $\sim 70^\circ$. From our teleseismic analysis and subsequent two-layer modeling for which we fixed the anisotropic properties of upper layer based on the characteristics of the local faults, we infer that the bulk anisotropic fast axis is oriented roughly parallel to the motion of the plate, with a deviation from the APM of $\sim 15^\circ$. Minor changes of fast polarizations between the stations can be explained by the effect of different upper-layer parameters depending on the strike of faults in the vicinity of the stations. Overprinting of the fossilized anisotropic fabric by fault-induced slab hydration (Faccenda et al., 2008) or extension (Eakin et al., 2016), which would affect the upper part of the subducting plate and lead to a mostly trench-parallel anisotropic fabric for this part of the subduction system, are not consistent with our data as shown by the direct observations and the inversion and the modeling. If it were present beneath the slab, its effects are likely canceled out by a much stronger anisotropic layer with trench-perpendicular fast axis (the lower-layer in our modeling).

The thickness of the subducting slab below the IPOC stations is estimated to be ~ 50 km (Sodoudi et al., 2011). Using an average mantle S wave velocity of 4.6 km/s, the slab would need to have 10% anisotropy to explain the mean observed teleseismic delay times of 1.1 s. As this is rather high, we instead assume an average value of 4% mantle anisotropy and estimate the thickness of the anisotropic fabric to be ~ 127 km. Thus, the mantle below the slab must contribute significantly to the observed splitting measurements. However, we have neglected the effect of the dip of the anisotropic fast axis which results from the subduction of the plate and possibly entrained flow. For dips greater than 30° , variations of splitting parameters with backazimuth may occur and should especially be evident in delay times. For most of our station locations which are mainly situated atop the fore-arc, the slab dip is $\sim 15^\circ$ except for the northern part, where the subduction becomes gradually steeper. Thus, its effect on our measurements is considered not significant. Our findings of trench-normal fast polarization directions at depth are corroborated by Song and Kawakatsu (2012) for shallowly dipping slabs.

5.2. Comparison to other studies

The shear-wave splitting analysis at the 21 stations of the IPOC network does not yield evidence for trench-parallel mantle flow

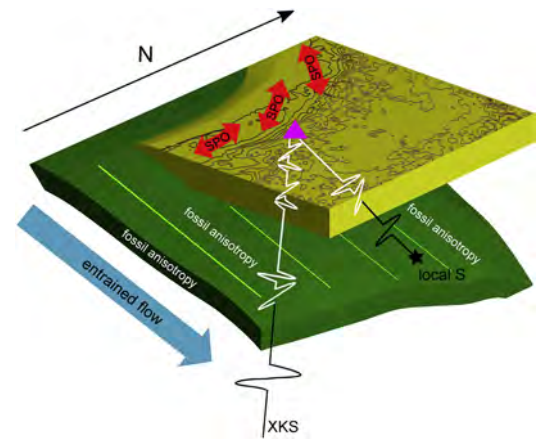


Fig. 8. Sketch of the final model of anisotropy in the Nazca subduction system. Trench-perpendicular fast-axes are caused by fossilized anisotropy within the slab and possible entrainment of mantle flow parallel to the APM. Anisotropy in the upper layer is located within the overriding plate and is attributed to local faults zones (SPO), which are partly parallel to the trench.

due to trench rollback, as was previously suggested for this part of the Nazca subduction zone (Russo and Silver, 1994; Bock et al., 1998). Our study covers a significantly larger area in contrast to previous studies that focused on a more-narrow zone between $18\text{--}20^\circ\text{S}$ where East–West fast polarizations occur (Polet et al., 2000), an area which was thought to represent a stagnation point or zone from which the mantle flow field moved to the North and South parallel to the trench (Russo and Silver, 1994). As has previously been suggested for the center of the study area at 21° (Wölbern et al., 2014), fossilized anisotropy located within the subducting slab and oriented in the direction of absolute plate motion can explain the bulk of the observed teleseismic shear-wave splitting measurements. This study also included a slab dip of 30° . North of our study area, Eakin and Long (2013) and Eakin et al. (2015) observed complex and depth-dependent anisotropy from shear-wave splitting of multiple seismic phases, which suggested a component of trench-normal mantle flow beneath the subducting slab. Long et al. (2016) also detected layered anisotropy (see Fig. 5) but argued for a trench-parallel anisotropic fabric beneath the slab possibly due to toroidal mantle flow from slab rollback. Following our analysis, we suggest that the observed trench-perpendicular fast polarizations stem from a combination of fossilized anisotropy within the slab and entrained downward mantle flow below it. This is also corroborated by the findings of Hicks et al. (2012) further south.

Our results have important implications for the geodynamic subduction process: using realistic parameters, the modeling of large-scale trench-parallel flow beneath subducting slabs has previously proven to be difficult (Alisic et al., 2012; Lowman et al., 2007). This is corroborated by the analysis presented here, which yields a more-straightforward and simple geodynamic interpretation. Given the central location of the IPOC stations along the Nazca subduction system and the complicated splitting patterns elsewhere along the margin, different mantle-flow patterns and mechanisms may be feasible when moving away from the center of the subducting plate. Our final model consists of a lower anisotropic layer representing the (combined) effects of the slab and the possible entrained mantle flow, and an upper (crustal) layer of seemingly trench-parallel fast axes that can be attributed to local fault zones which accommodate the crustal thickening of the overriding plate in response to the subduction (Fig. 8). The possible influence of the mantle wedge in the North is omitted in view of the good fit between fast polarization from local S phases and the strike of the faults in all other parts of the study area and the small magnitude of its influence.

6. Conclusion

In this study, we use shear-wave splitting analysis from teleseismic XKS and local S phases to constrain the anisotropic properties of the Nazca subduction system in the central Andes. We analyze more than 10 yrs of data from 21 stations of IPOC network (GFZ, 2006), which are located in the fore-arc region between 17°–25°S (Fig. 1) and provide a unique data set to study this subduction system. We show that shear-wave splitting results are best characterized by two anisotropic layers: a roughly APM-parallel lower layer (diverging by ~15° from the estimated plate motion) and a heterogeneous upper layer. The upper layer is well constrained by the ray paths and properties of the shear-wave splitting measurements of local S phases. We interpret this layer to be related to local fault zones which accommodate the crustal thickening during the subduction process. The anisotropic properties of the lower layer are inferred from the teleseismic analysis which we resolve by fixing the anisotropy of the upper layer to resemble the strike of fault zones in the crust.

Our observations do not corroborate the existence of trench-parallel mantle flow beneath our study area. The slab also seems to retain its anisotropic properties from the time of plate formation. Additionally, the mantle wedge does not play a significant role. Thus, the data suggest that the dynamics of the subduction zone at depth can be explained by the simple and straightforward model of mantle flow parallel to the down-dip direction of subduction.

Acknowledgements

This study was supported by the Deutsche Forschungsgemeinschaft (DFG) with grants to MCR (RU 886/11-1) and IW (WO 1723/1-2). The data is archived at GEOFON (GFZ, 2006) and can be accessed at <https://doi.org/10.14470/PK615318>. SplitRacer is a free software package for teleseismic shear-wave splitting analysis and can be downloaded here: <http://www.geophysik.uni-frankfurt.de/64002762/Software>. Maps were visualized with the GMT software (Wessel and Smith, 1998).

Appendix A. Supplementary material

Supplementary material related to this article can be found online at <https://doi.org/10.1016/j.epsl.2017.11.002>.

References

Alisic, L., Gurnis, M., Stadler, G., 2012. Multi-scale dynamics and rheology of mantle flow with plates. *J. Geophys. Res.* 117, B10402.

Allmendinger, R.W., Gubbels, T., 1996. Pure and simple shear plateau uplift, Altiplano-Puna, Argentina and Bolivia. *Tectonophysics* 259, 1–13.

Anderson, M.L., Zandt, G., Triep, E., Fouch, M., Beck, S., 2004. Anisotropy and mantle flow in the Chile–Argentina subduction zone. *Geophys. Res. Lett.* 31, L23608. <https://doi.org/10.1029/2004GL020906>.

Becker, T.W., Conrad, C.P., Schaeffer, A.J., Lebedev, S., 2014. Origin of azimuthal seismic anisotropy in oceanic plates and mantle. *Earth Planet. Sci. Lett.* 401, 236–250.

Bock, G., Kind, R., Rudloff, A., Asch, G., 1998. Shear wave anisotropy in the upper mantle beneath the Nazca plate in northern Chile. *J. Geophys. Res.* 103, 24333–24345.

Bostock, M.G., Hyndman, R.D., Rondenay, S., Peacock, A.M., 2002. An inverted continental Moho and serpentinization of the forearc mantle. *Nature* 417, 536–538. <https://doi.org/10.1038/417536a>.

Brasse, H., Eydam, D., 2008. Electrical conductivity beneath the Bolivian Orocline and its relation to subduction processes at the South American continental margin. *J. Geophys. Res.* 113, B07109. <https://doi.org/10.1029/2007JB005142>.

Cahill, T., Isacks, B.L., 1992. Seismicity and shape of the subducted Nazca plate. *J. Geophys. Res.* 97, 17503–17529.

Charrier, R., Hérail, G., Pinto, L., García, M., Riquelme, R., Farías, M., Muñoz, N., 2013. Cenozoic tectonic evolution in the Central Andes in northern Chile and

west central Bolivia: implications for paleogeographic, magmatic and mountain building evolution. *Int. J. Earth Sci.* 102, 235–264. <https://doi.org/10.1007/s00531-012-0801-4>.

Crampin, S., 1994. The fracture criticality of crustal rocks. *Geophys. J. Int.* 118, 428–438.

Eakin, C.M., Long, M.D., 2013. Complex anisotropy beneath the Peruvian flat slab from frequency dependent, multiple-phase shear wave splitting analysis. *J. Geophys. Res., Solid Earth* 118, 4794–4813. <https://doi.org/10.1002/jgrb.50349>.

Eakin, C.M., Long, M.D., Wagner, L.S., Beck, S.L., Tavera, H., 2015. Upper mantle anisotropy beneath Peru from SKS splitting: constraints on flat slab dynamics and interaction with the Nazca Ridge. *Earth Planet. Sci. Lett.* 412, 152–162. <https://doi.org/10.1016/j.epsl.2014.12.015>.

Eakin, C.M., Long, M.D., Scire, A., Beck, S.L., Wagner, L.S., Zandt, G., Tavera, H., 2016. Internal deformation of the subducted Nazca slab inferred from seismic anisotropy. *Nat. Geosci.* 9, 56–59. <https://doi.org/10.1038/ngeo2592>.

Faccenda, M., Burlini, L., Gerya, T.V., Mainprice, D., 2008. Fault-induced seismic anisotropy by hydration in subducting oceanic plates. *Nature* 455, 1097–1100.

Fouch, M.J., Rondenay, S., 2006. Seismic anisotropy beneath stable continental interiors. *Phys. Earth Planet. Inter.* 158, 292–320. <https://doi.org/10.1016/j.pepi.2006.03.024>.

García, M., Gardeweg, M., Clavero, J., Hérail, G., 2004. Hoja Arica, Región de Tarapacá. In: *Carta geológica de Chile. In: Serie Geológica Básica, vol. 84.*

GFZ German Research Centre for Geosciences, Institut des Sciences de l'Univers-Centre National de la Recherche CNRS-INSU, 2006. IPOC Seismic Network. Integrated Plate boundary Observatory Chile – IPOC. <https://doi.org/10.14470/PK615318>.

Hess, H., 1964. Seismic anisotropy of the uppermost mantle under oceans. *Nature* 203, 629–631.

Hicks, S.P., Nippres, S.E.J., Rietbrock, A., 2012. Sub-slab mantle anisotropy beneath south-central Chile. *Earth Planet. Sci. Lett.* 357–358, 203–213. <https://doi.org/10.1016/j.epsl.2012.09.017>.

Jung, H., Karato, S., 2001. Water-induced fabric transition in olivine. *Science* 293, 1460–1463.

Karato, S., Wu, P., 1993. Rheology of the upper mantle: a synthesis. *Science* 260, 771–778.

Ko, B., Jung, H., 2015. Crystal preferred orientation of an amphibole experimentally deformed by simple shear. *Nat. Commun.* 6, 6586. <https://doi.org/10.1038/ncomms7586>.

Long, M.D., Silver, P., 2008. The subduction zone flow field from seismic anisotropy: a global view. *Science* 319, 315–318.

Long, M.D., Silver, P.G., 2009a. Mantle flow in subduction systems: the subslab flow field and implications for mantle dynamics. *J. Geophys. Res.* 114, B10312. <https://doi.org/10.1029/2008JB006200>.

Long, M.D., Silver, P.G., 2009b. Shear wave splitting and mantle anisotropy: measurements, interpretations, and new directions. *Surv. Geophys.* 30, 407–461.

Long, M.D., Biryol, C.B., Eakin, C.M., Beck, S.L., Wagner, L.S., Zandt, G., Minaya, T.E., Tavera, H., 2016. Overriding plate, mantle wedge, slab, and subslab contributions to seismic anisotropy beneath the northern Central Andean Plateau. *Geochem. Geophys. Res.* 17, 2556–2575.

Lowman, J.P., Pinero-Feliciangeli, L.T., Kendall, J.M., Hosein Shahnas, M., 2007. Influence of convergent plate boundaries on upper mantle flow and implications for seismic anisotropy. *Geochem. Geophys. Res.* 12, Q08007.

MacDougall, J.G., Fischer, K.M., Anderson, M.L., 2012. Seismic anisotropy above and below the subducting Nazca lithosphere in southern South America. *J. Geophys. Res.* 117, B12306. <https://doi.org/10.1029/2012JB009538>.

Ohuchi, T., Kawazoe, T., Nishihara, Y., Irifune, T., 2012. Change of olivine a-axis alignment induced by water: origin of seismic anisotropy in subduction zones. *Earth Planet. Sci. Lett.* 317–318, 111–119.

Özalaybey, S., Savage, M.K., 1994. Double-layer anisotropy resolved from S phases. *Geophys. J. Int.* 117, 653–664.

Park, J., Levin, V., 2002. Seismic anisotropy: tracing plate dynamics in the mantle. *Science* 296, 485–489.

Polet, J., Silver, P.G., Beck, S., Wallace, T., Zandt, G., Ruppert, S., Kind, R., Rudloff, A., 2000. Shear wave anisotropy beneath the Andes from BANJO, SEDA, and PISCO experiments. *J. Geophys. Res.* 105, 6287–6304.

Reiss, M.C., Rumpker, G., 2017. SplitRacer: MATLAB code and GUI for semiautomated analysis and interpretation of teleseismic shear-wave splitting. *Seismol. Res. Lett.* 88 (2A), 392–409.

Reutter, K.-J., Munier, K., 1994. Digital geological map of the Central Andes between 20°S and 26°S. In: Reutter, K.-J., et al. (Eds.), *Tectonics of the Southern Andes*. Heidelberg.

Rumpker, G., Silver, P.G., 1998. Apparent shear-wave splitting parameters in the presence of vertically-varying anisotropy. *Geophys. J. Int.* 135, 790–800.

Rumpker, G., Ryberg, T., Bock, G., Desert Seismology Group, 2003. Boundary-layer mantle flow under the Dead Sea transform fault inferred from seismic anisotropy. *Nature* 425, 497–501.

Russo, R.M., Silver, P.G., 1994. Trench-parallel flow beneath the Nazca plate from seismic anisotropy. *Science* 263, 1105–1111.

Savage, M.K., 1999. Seismic anisotropy and mantle deformation: what have we learned from shear wave splitting? *Rev. Geophys.* 37, 65–106.

- Silver, P.G., Chan, W., 1991. Shear wave splitting and subcontinental mantle deformation. *J. Geophys. Res.* 96, 16429–16454.
- Silver, P.G., Savage, M.K., 1994. The interpretation of shear-wave splitting parameters in the presence of two anisotropic layers. *Geophys. J. Int.* 119, 949–963.
- Sodoudi, F., Yuan, X., Asch, G., Kind, R., 2011. High-resolution image of the geometry and thickness of the subducting Nazca lithosphere beneath northern Chile. *J. Geophys. Res.* 116, B04302. <https://doi.org/10.1029/2010JB007829>.
- Song, T.-R.A., Kawakatsu, H., 2012. Subduction of oceanic asthenosphere: evidence from sub-slab seismic anisotropy. *Geophys. Res. Lett.* 39, L17301. <https://doi.org/10.1029/2012GL052639>.
- Veloza, G., Styron, R., Taylor, M., Mora, A., 2012. Active tectonics of the Andes: an open-source archive for active faults in northwestern South America. *GSA Today* 22 (10), 4–10. <https://doi.org/10.1130/GSAT-G156A.1>.
- Walpole, J., Wookey, J., Kendall, J.-M., Masters, T.-G., 2017. Seismic anisotropy and mantle flow below subducting slabs. *Earth Planet. Sci. Lett.* 465, 155–167. <https://doi.org/10.1016/j.epsl.2017.02.023>.
- Wessel, P., Smith, W.H.F., 1998. New, improved version of the generic mapping tools released. *Eos Trans. AGU* 79, 579. <https://doi.org/10.1029/98EO00426>.
- Wölbern, I., Heit, B., Yuan, X., Asch, G., Kind, R., Viramonte, J., Tawackoli, S., Wilke, H., 2009. Receiver function images from the Moho and the slab beneath the Altiplano and Puna plateaus in the Central Andes. *Geophys. J. Int.* 177, 296–308.
- Wölbern, I., Löbl, U., Rümpker, G., 2014. Crustal origin of trench-parallel shear wave fast polarizations in the Central Andes. *Earth Planet. Sci. Lett.* 392, 230–238.
- Wolfe, C.J., Silver, P.G., 1998. Seismic anisotropy of oceanic upper mantle: shear-wave splitting methodologies and observations. *J. Geophys. Res.* 103, 749–771.
- Zhang, S., Karato, S., 1995. Lattice preferred orientation of olivine aggregates deformed by simple shear. *Nature* 375.